

The vertical gradient response ( $dG_z/dz$ ) is shown in Figure 10, and the difference between 2020 and initial conditions is shown in Figure 11. The change in the response is about 10 EU, which is easily measured. The reservoir is between 1325 and 1350 m outlined in blue.

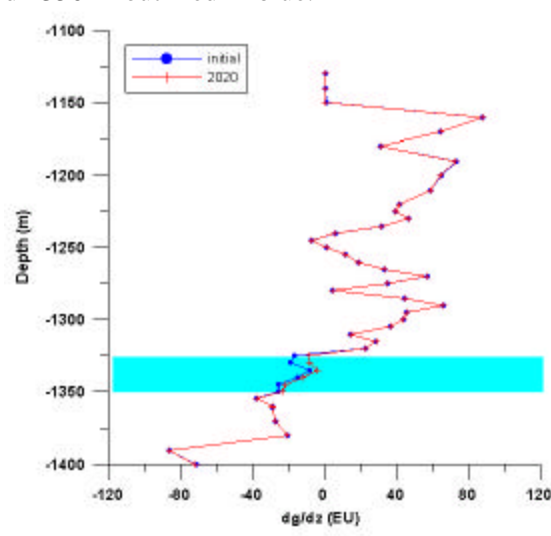


Figure 10: Borehole vertical gradient response ( $dG_z/dz$ ) for initial conditions (blue) and 2020 (red).

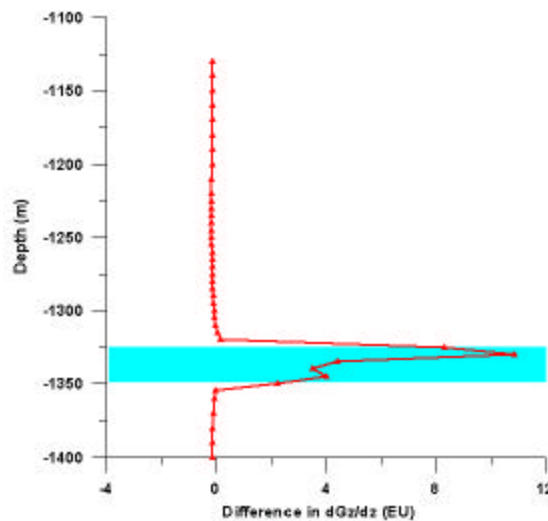


Figure 11: Difference between vertical gradient response ( $dG_z/dz$ ) in 2020 and initial conditions.

Popta et al. (1990) showed that a geological structure with a sufficient density contrast can be detected by borehole gravity measurements if the observation well is not further away than one or two times the thickness of the anomalous zone. This means that borehole gravity could be used to detect CO<sub>2</sub>-water saturation changes up to 60m away from the borehole in this case.

If the amount of water or CO<sub>2</sub> injected into the formation is significant enough to cause a change in the density, gravity measurements will respond. The gravity response due to water flood will increase, while if CO<sub>2</sub> is injected the gravity response will decrease. In the case of Schrader Bluff, where there is a combination of water and CO<sub>2</sub> injection the final response will depend on the relative position in the reservoir of these two component.

### 2.4.2.6.2 Seismic modeling:

We have an on-going effort in seismic modeling for Schrader Bluff. The flow simulation models have been converted to acoustic and shear velocity (in addition to density). A simulated seismic line has been calculated running approximately N45E across the reservoir. The elastic response to a 50 Hz Ricker wavelet has been calculated. The increase in CO<sub>2</sub> saturation produces approximately a 20% decrease in seismic velocity as shown in Figure 12 (a difference in P-wave velocity between 2005 and 2020). The CO<sub>2</sub> saturation and water saturation changes are shown in Figures 13 and 14 respectively. The seismic responses, for a single shot located at 7500 m (covering the area of the reservoir with maximum CO<sub>2</sub> saturation change) on the 2D profile, for 2005 and 2020 are shown in Figure 15 with the difference shown in Figure 16.

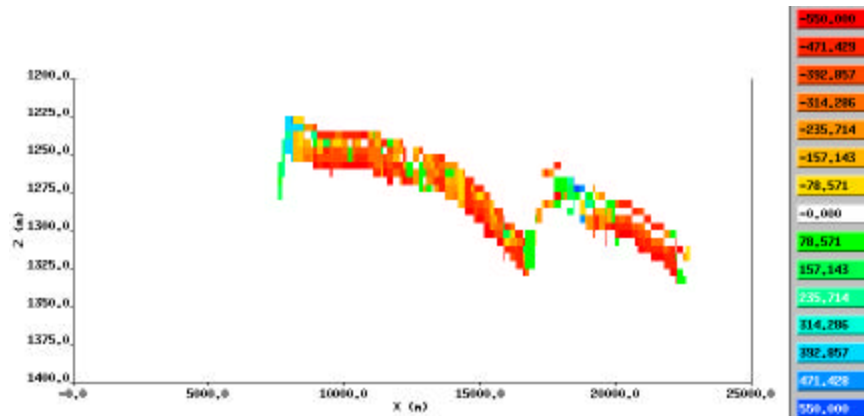


Figure 12: Difference in the acoustic velocity ( $V_p$ ) between 2020 and 2005 along a 2D profile extracted from the 3D model volume. The profile runs N45E across the 3D model. Note the significant decrease in acoustic velocity associated with the increase in CO<sub>2</sub> saturation (Figure 13).

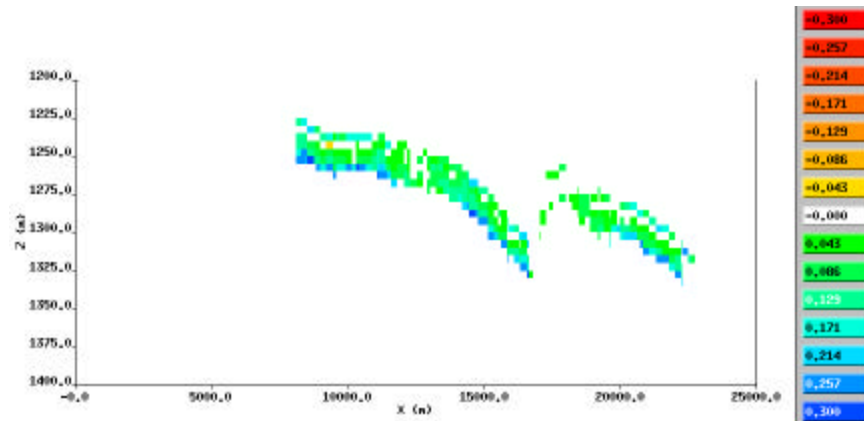


Figure 13: Difference in the CO<sub>2</sub> saturation between 2020 and 2005.

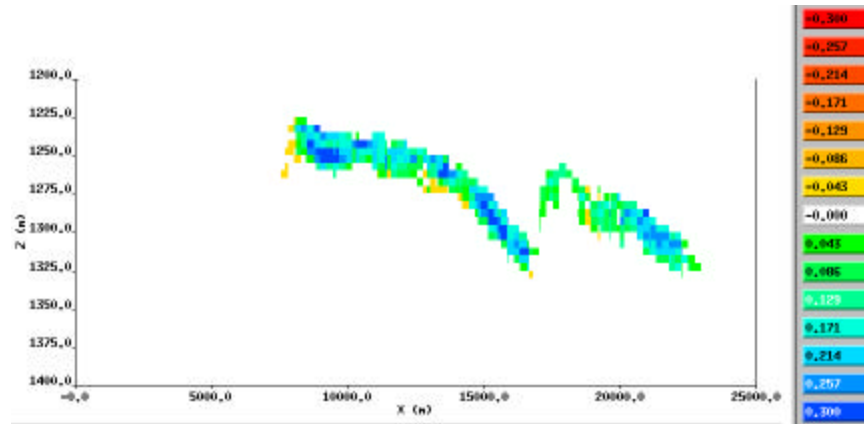


Figure 14: Difference in the water saturation between 2020 and 2005.

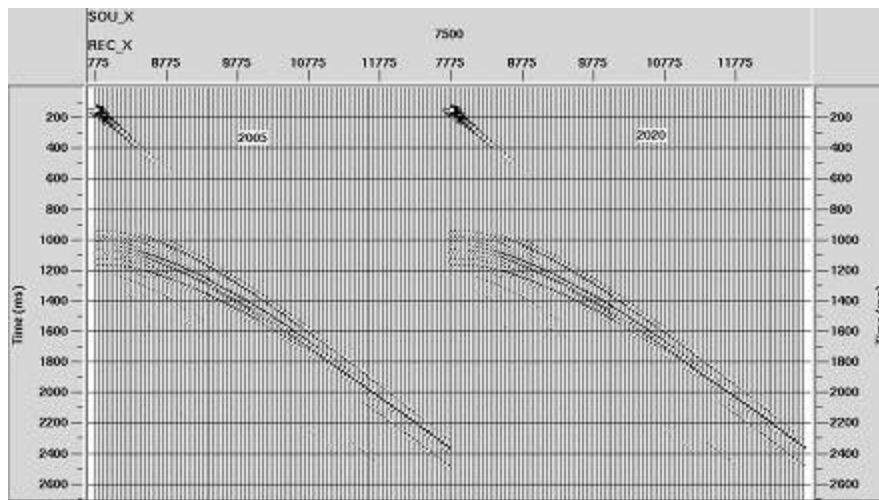


Figure 15: Seismic response (shot gather) for 2005 and 2020.

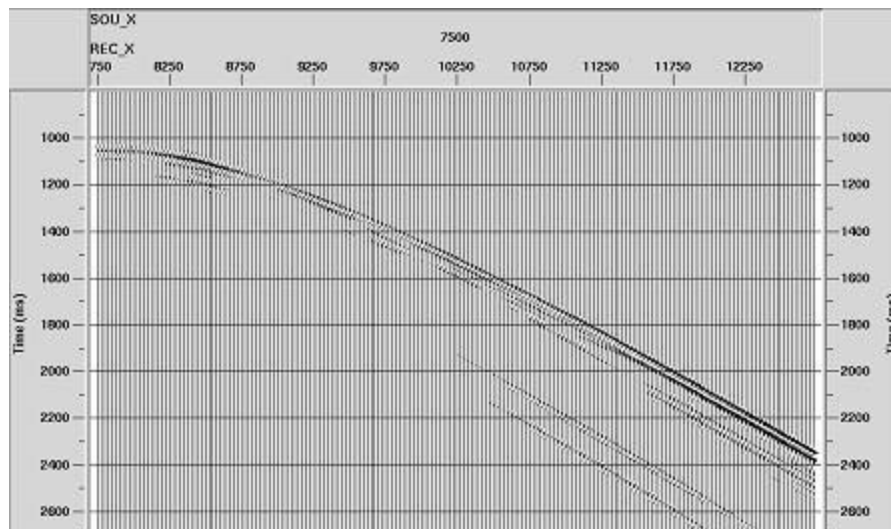


Figure 16: Difference in seismic response (shot gather) between 2020 and 2005. Note amplitude change and AVO effects associated with water and CO<sub>2</sub> saturation changes in the reservoir.

Figure 17a and 17b show the P-wave velocity ( $V_p$ ) field as a function of distance along the profile (m) and time (ms) for a time-snap at 2005 and 2020, respectively. Blue colors represent low velocities, while red colors represent high velocities. At 2005 time-snap there are only patchy areas where the velocity

decreases due to the presence of CO<sub>2</sub>, while at 2020, we can see that the velocity decrease is continuous at the top part of the reservoir (~970 ms).

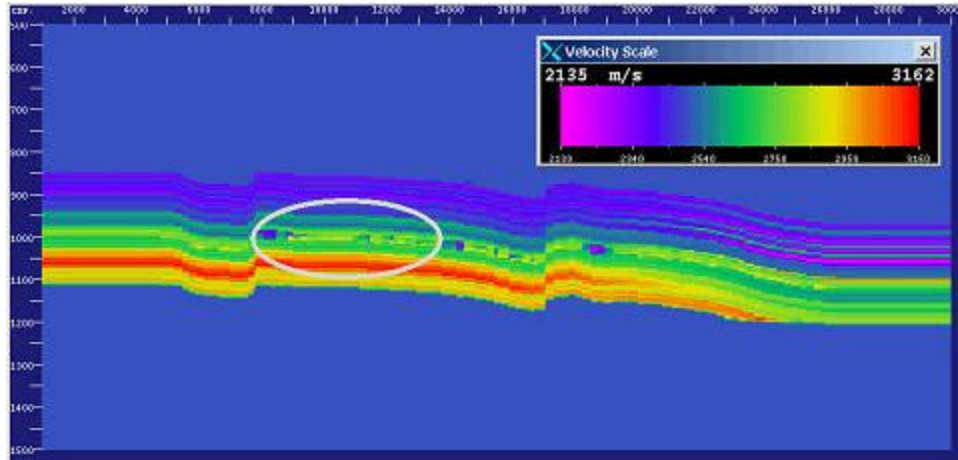


Figure 17a: Velocity field as a function of x along the profile (m) and time (ms) for 2005.

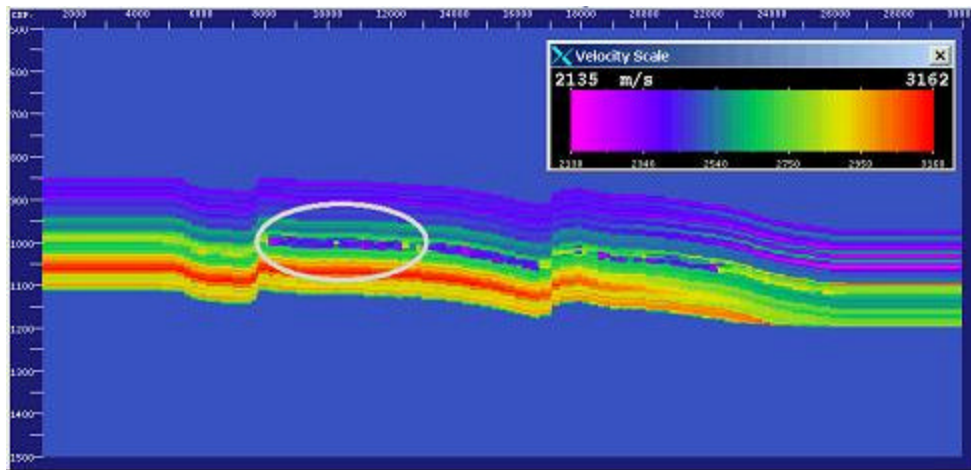


Figure 17b: Velocity field as a function of x along the profile (m) and time (ms) for 2020.

Stacked sections for both years (2005 and 2020) are shown in Figure 18. The profile in the stack section for 2020 is shorter than 2005, however they both cover the area of interest between 8,000 and 16,000 m, where the major change in the response due to CO<sub>2</sub> occurs.

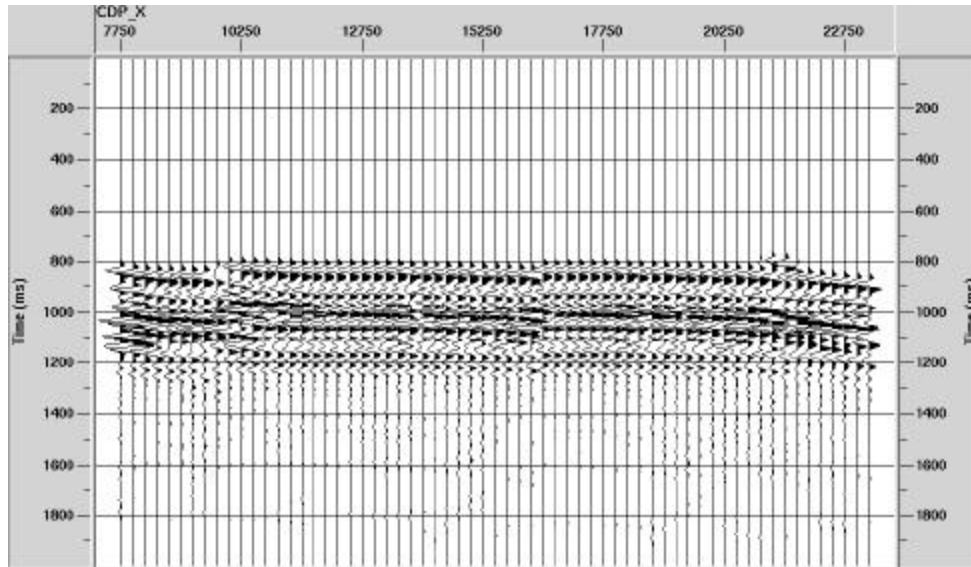


Figure 18a: **Stacked time section for 2005.**

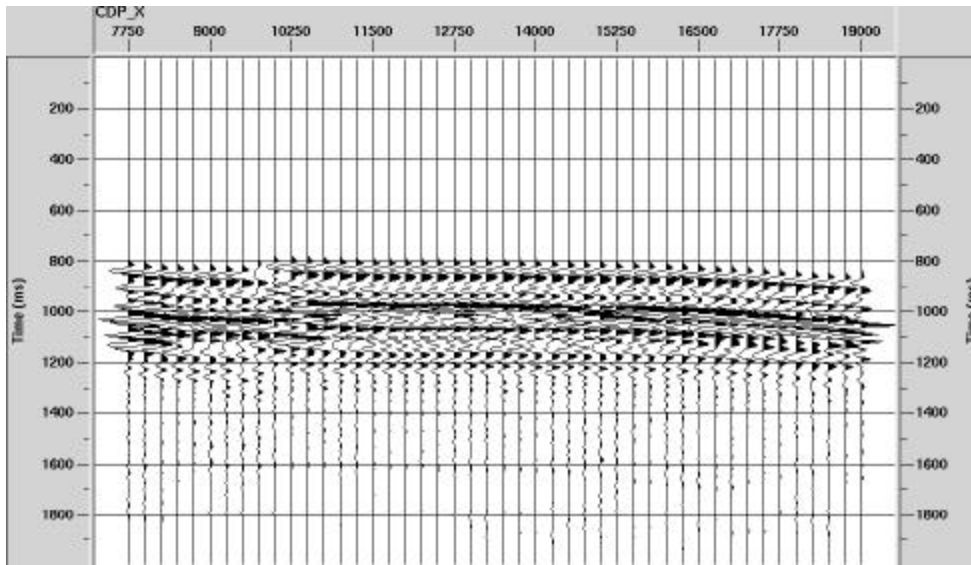


Figure 18b: **Stacked time section for 2020.**

For our analysis we focused on the middle part of the profile, which is indicated by a white ellipse. Angle stacked sections for these two years are shown in Figure 19. The red line indicates the place where changes due to CO<sub>2</sub> presence occur.

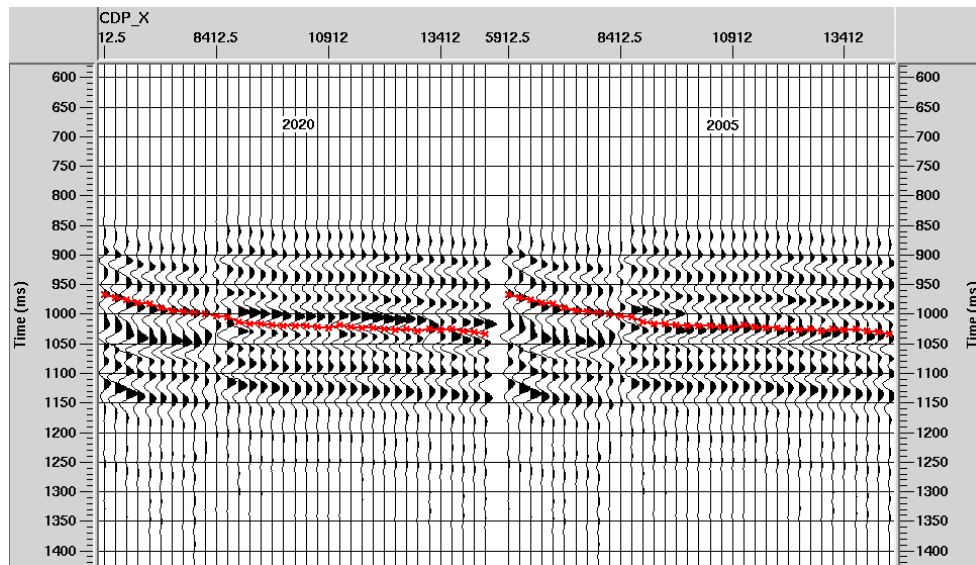


Figure 19: Angle stacked section for 2005 and 2020.

The difference in stack section between 2005 and 2002 is shown in Figure 20. There is a very little change on the left side of the profile and in area around  $x = 13,000$ , where there was no  $\text{CO}_2$  present in either time. The main difference in the response is between  $x = 9,500$  and  $13,000$ .

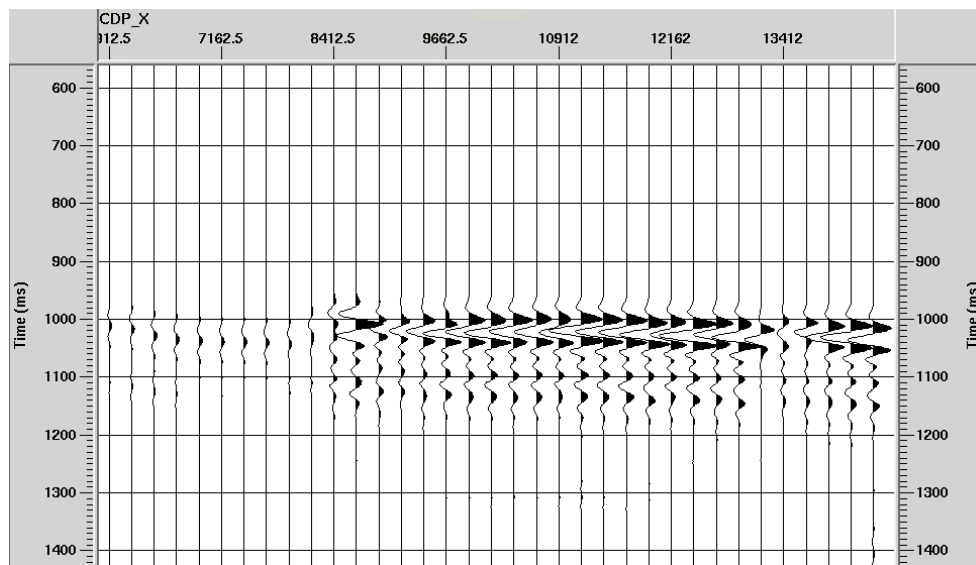


Figure 20: Difference in stack section between 2020 and 2005 (2020-2005).

There is a clear change in stacked trace amplitude associated with the reservoir caused by the changes in water and  $\text{CO}_2$  saturation. In addition, there is a change in the AVO effects. Both amplitude and AVO can be exploited to make quantitative estimates of saturation changes. We have developed an AVO inversion technique for estimating saturations from AVO data that will be applied to the synthetic data by the completion of the project. Forward calculations using Zoeppritz equation for both 2005 and 2020 model have been done to understand the AVO dependence on the parameters of the model. The forward modeling creates a synthetic seismic gather from a given set of elastic parameters  $V_p$ ,  $V_s$  and density in depth as summarized in Figure 21.

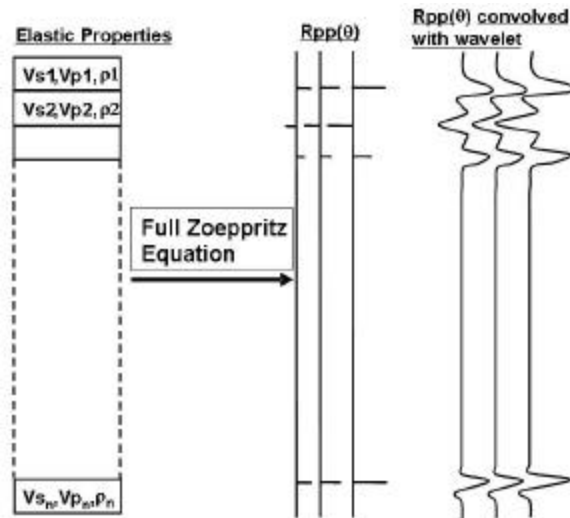


Figure 21: **Workflow for seismic synthetic modeling**

The full Zoeppritz equation is used to compute the reflection coefficient  $Rpp(\theta)$  for each angle and at each layer boundary. Synthetic offset seismic gathers are calculated by convolving the reflection coefficients with predetermined wavelets. A 50Hz Ricker wavelet was used in this study. The convolution model assumes plane-wave propagation across the boundaries of horizontally homogeneous layers, and takes no account of the effects of geometrical divergence, inelastic absorption, wavelet dispersion, transmission losses, mode conversions and multiple reflections. In addition to the plane-wave approximations we can model the full 3D anisotropic-elastic effects over the Schrader Bluff model (currently on-going) and will compare these to the 1D approximations.

The difference in  $Vp$ ,  $Vs$ , and density is shown in Figure 22. The reservoir is between 1250 m and 1275 m.

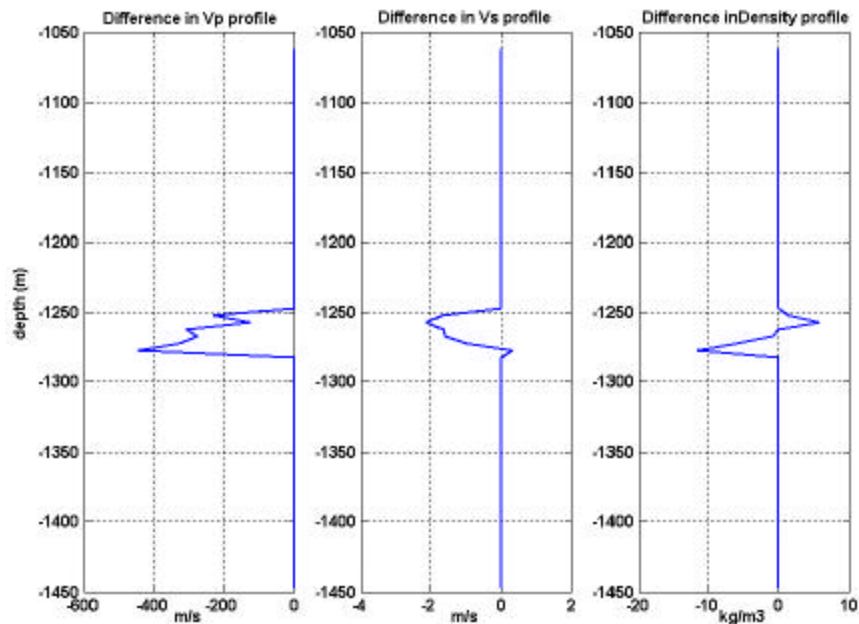


Figure 22: **Difference in  $Vp$ ,  $Vs$ , and density profiles between 2005 and 2020 for the Schrader Bluff model at the center of maximum  $CO_2$  saturation increase.**

The synthetic gather as a function of angle for 2005 is shown in Figure 23 while the gather for 2020 is shown in Figure 24. Because the gathers are scaled to the peak amplitude, it is very hard to compare these two figures. Instead, the difference between these two times, shown in Figure 25, shows a strong positive AVO response associated with the change in CO<sub>2</sub> and water saturations. In the final stages of the project these AVO responses will be inverted to predict the saturations as a way of quantifying how accurately one could expect saturation predictions to be.

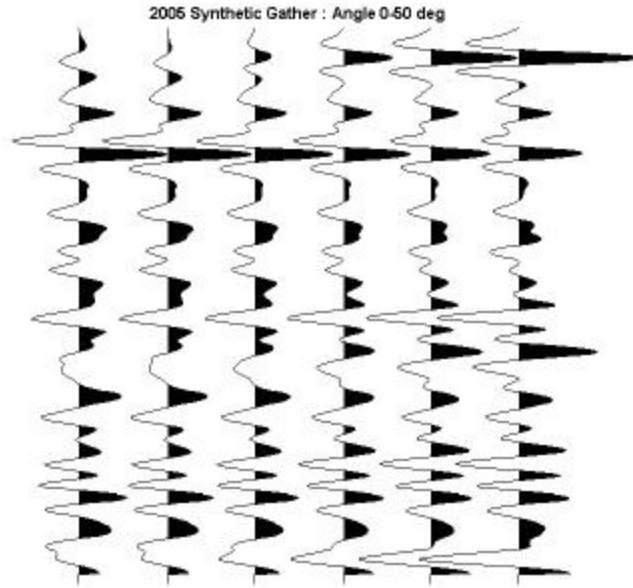


Figure 23: Synthetic gather for 2005 (scaled to peak maximum).

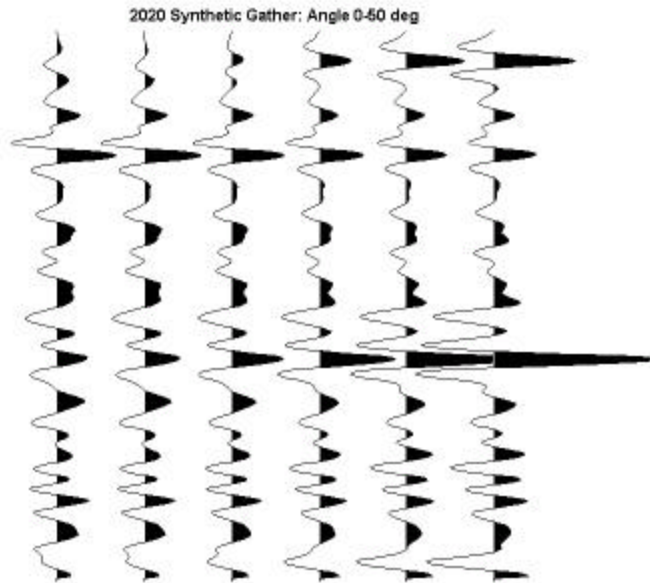


Figure 24: Synthetic gather for 2020 (scaled to peak maximum).



Figure 25: **Difference between 2020 and 2005 gathers.**

### 2.4.6.3 Laboratory studies

We have continued our laboratory studies on the streaming potential due to CO<sub>2</sub> injection in Berea sandstone (Lang Stone, Columbus, Ohio). These are the first such measurements for CO<sub>2</sub> to our knowledge, and will be the subject of a separate paper now in preparation. The testing device holds a 127 mm long core of 25 mm diameter (Figure 26). Tests were run on two different rock samples. Each sample was saturated prior to testing under vacuum for a period no less than 1 day. The pore fluid for initial saturation was normal tap water, tested to have a resistivity of 125 Ohm-m. The coupling coefficient for the rock/water case was determined both before and after each CO<sub>2</sub> flood of two samples using a low-pressure static head method. Next, liquid CO<sub>2</sub> was allowed to flow over each sample. Test 1 allowed liquid CO<sub>2</sub> to flow through the sample for 1½ hour, while test 2 lasted 1 hour.

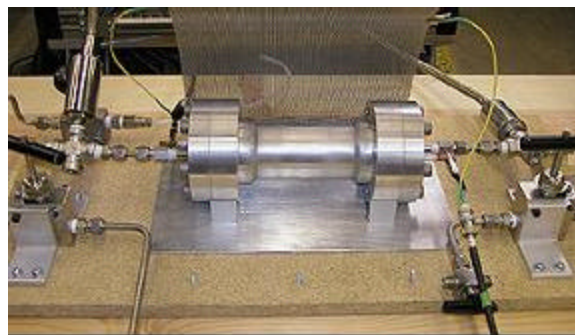


Figure 26: **Testing device containing Berea sandstone core. Sample is 127 mm long and 25 mm diameter.**

Figure 27 illustrates that the observed potentials and applied pressure drop correlated well throughout the testing.

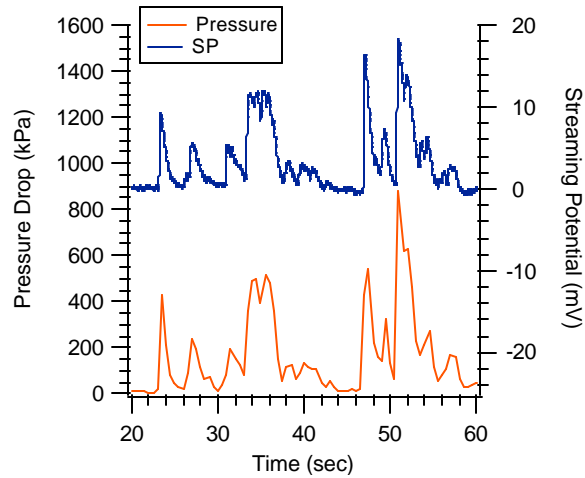


Figure 27: Streaming potential and pressure drop as a function of time as CO<sub>2</sub> is injected into the core sample.

Prior to each CO<sub>2</sub> injection, coupling coefficient information was determined for the Berea sandstone sample saturated with 125 Ohm-m tap water. For these low-pressure tests, results indicate linear correlation of applied pressure and observed potential, as illustrated in Figure 28.

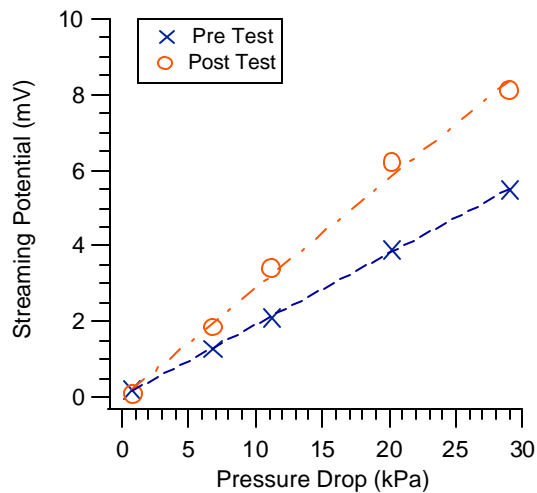


Figure 28: Results for static head testing to determine water-only coupling coefficient both prior to and following CO<sub>2</sub> injection test 2. Resistivity of pore fluid was 125 Ohm-m. Slope of line indicates coupling coefficients of 20 mV/0.1MPa (Pre) and 30 mV/0.1MPa (Post).

When liquid CO<sub>2</sub> was applied to the sample, the water in the sample pore space was displaced, while reacting with the CO<sub>2</sub> to form carbonic acid. The coupling coefficient evolved over time in response to the mixing and displacing of the pore water. Figure 29 shows the coupling coefficient evolution of both tests for the 20 minutes following CO<sub>2</sub> injection.

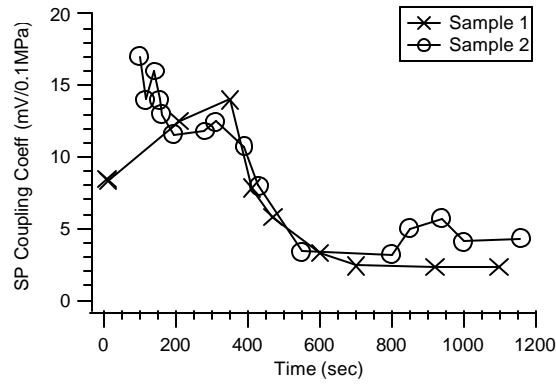


Figure 29: Coupling coefficients as a function of time for the first 20 minutes of CO<sub>2</sub> injection for samples 1 and 2. Coupling coefficient values were steady for times greater than 700 seconds, and remained steady throughout the remaining testing time.

The results of the test are summarized in Table 1. As the CO<sub>2</sub> displaced the water the coupling coefficient decreased. On average, the coupling coefficients observed for CO<sub>2</sub> flow is about 10 times lower than for water flow in the same sample. Since the liquid CO<sub>2</sub> coupling coefficient is smaller than that of water, the most effective way to spatially monitor injected CO<sub>2</sub> flow is to monitor the progressing CO<sub>2</sub>/water front, where the coupling coefficient is largest.

Table 1: Summary of coupling coefficient results. All units are in mV/0.1MPa.

	<i>Pre-Test (water)</i>	<i>During (CO<sub>2</sub>)</i>	<i>Post-Test (water)</i>
<i>Sample 1</i>	45	2.5	15
<i>Sample 2</i>	20	3.5	30

## 2.4.2.7 Results and Discussion

Although the magnitude of the surface gravity response (3 mGal) is about an order of magnitude above the gravimeter sensitivity, and therefore measurable in the field, the difference caused by CO<sub>2</sub> injection is only about 0.5 μGal, which is in the noise level of the field survey (Hare, 1999). The negative change in the response is caused by increased CO<sub>2</sub> saturations reducing the bulk density of the reservoir. The change in the vertical gradient of gravity has a strong correlation with the gradient of the change in pressure in the reservoir. Again, the magnitude of the signal measured in the field (2–10 EU) is above the gradiometer accuracy (0.5–1 EU), but the difference between initial conditions and 5 years into CO<sub>2</sub> injection is very small (~0.005 EU). If the noise levels of measurements of the changes in dG<sub>z</sub>/dz could be reduced by permanent sensor emplacement and continuous monitoring gravity and gradient measurements may offer a tool for monitoring.

The difference in both borehole gravity response and vertical gravity gradient (dG<sub>z</sub>/dz) identifies the position of the reservoir. The sign of the change reflects the changes in the local densities caused by either water or CO<sub>2</sub>.

There is a clear change in seismic amplitude associated with the reservoir caused by the changes in water and CO<sub>2</sub> saturation. In addition, there is a change in the seismic AVO effects. Both seismic amplitude and AVO can be exploited to make quantitative estimates of saturation changes. Forward calculations using Zoeppritz equation for both 2005 and 2020 models support this argument. We have developed an AVO inversion technique for estimating saturations from AVO data that will be applied to the synthetic data set in future work.

Laboratory studies showed that the coupling coefficients for CO<sub>2</sub> are large enough to cause SP signal measurable in the field. As the CO<sub>2</sub> displaces the water the coupling coefficient decreases. On average, the coupling coefficients observed for CO<sub>2</sub> flow is about 10 times lower than for water flow in the same sample. Since the liquid CO<sub>2</sub> coupling coefficient is smaller than that of water, the most effective way to spatially monitor injectate flow is to monitor the progressing CO<sub>2</sub>/water front, where the coupling coefficient is largest.

## 2.4.2.8 Conclusion

Although the magnitude of the surface gravity response (3 mGal) is about an order of magnitude above the gravimeter sensitivity, and therefore measurable in the field, the difference caused by CO<sub>2</sub> injection is only about 0.5 μGal, which is in the noise level of the field survey (Hare, 1999). The negative change in the response is caused by increased CO<sub>2</sub> saturations reducing the bulk density of the reservoir. The change in the vertical gradient of gravity has a strong correlation with the gradient of the change in pressure in the reservoir. Again, the magnitude of the signal measured in the field (2–10 EU) is above the gradiometer accuracy (0.5–1 EU), but the difference between initial conditions and 5 years into CO<sub>2</sub> injection is very small (~0.005 EU). If the relationship between pressure changes in the reservoir and the changes in  $dG_z/dz$  are validated, it offers an obvious tool for monitoring if  $dG_z/dz$  sensitivities can be increased.

The difference in both borehole gravity response and vertical gravity gradient ( $dG_z/dz$ ) identifies the position of the reservoir. The sign of the change reflects the changes in the local densities caused by either water or CO<sub>2</sub>.

There is a clear change in the seismic amplitude associated with the reservoir caused by the changes in water and CO<sub>2</sub> saturation. In addition, there is a change in the AVO effects. Both amplitude and AVO can be exploited to make quantitative estimates of saturation changes. Forward calculations using Zoeppritz equation for both 2005 and 2020 models support this argument. We have developed an AVO inversion technique for estimating saturations from AVO data that will be applied to the synthetic data set by the conclusion of the project.

Laboratory studies showed that the coupling coefficients for CO<sub>2</sub> are large enough to cause SP signal measurable in the field. As the CO<sub>2</sub> displaces the water the coupling coefficient decreases. On average, the coupling coefficients observed for CO<sub>2</sub> flow is about 10 times lower than for water flow in the same sample. Since the liquid CO<sub>2</sub> coupling coefficient is smaller than that of water, the most effective way to spatially monitor injectate flow is to monitor the progressing CO<sub>2</sub>/water front, where the coupling coefficient is largest.

## 2.4.2.9 References

Hare, J.L., Ferguson, J.F., and Aiken, C.L.V., 1999, The 4-D microgravity method for waterflood surveillance: A model study from the Prudhoe Bay reservoir, Alaska: *Geophysics*, **64**, p. 78-87.

Hoversten, G., M., Gritto, R., Washbourne, J., Daley, T., M., 2003, Pressure and Fluid Saturation Prediction in a Multicomponent Reservoir, using Combined Seismic and Electromagnetic Imaging. *Geophysics*, (In Press Sept-Oct 2003). LNBL - 51281

Popta, J.V., Heywood, J.M.T., Adams, S.J., and Bostock, D.R., 1990, Use of borehole gravimetry for reservoir characterization and fluid saturation monitoring: *SPE* 20896, p. 151- 160.

### **2.4.2.10 Publications**

Hoversten, G., M., Gritto, R., Washbourne, J., Daley, T., M., 2003, Pressure and Fluid Saturation Prediction in a Multicomponent Reservoir, using Combined Seismic and Electromagnetic Imaging. Geophysics, (In Press Sept-Oct 2003). LNBL - 51281

Hoversten. G. M., Gritto, R., Washbourne, J., Daley, T., , “Non-seismic geophysics for CO2 Sequestration Monitoring”, 2002 SEG Workshop on CO2 sequestration Oct. 10, 2002, SEG Annual Convention

Hoversten. G. M., Gritto, R., Washbourne, J., Daley, T., “CO2 gas/oil ratio prediction in a multi-component reservoir by combined seismic and electromagnetic imaging”, 2002, LBNL report # 51408

Hoversten, G. M., Myer, L., Daley, T., “Crosswell seismic and electromagnetic monitoring of CO2 sequestration”, 2002, GHGT-6 conference, Kyoto, Japan.

**2.4.2.13 Appendix A:**

**Pressure and Fluid Saturation Prediction in a Multicomponent Reservoir,  
using Combined Seismic and Electromagnetic Imaging**

**Presented at the SEG annual meeting, Oct 6-11, 2002, Salt  
Lake City, UT**

To be published in September 2003 in Geophysics

**G. M. Hoversten<sup>1</sup>  
Roland Gritto<sup>1</sup>  
John Washbourne<sup>2</sup>  
Tom Daley<sup>1</sup>**

<sup>1</sup> Lawrence Berkeley National Laboratory  
<sup>2</sup> TomoSeis Inc.

## **ABSTRACT**

*This paper presents a method for combining seismic and electromagnetic measurements to predict changes in water saturation, pressure, and CO<sub>2</sub> gas/oil ratio in a reservoir undergoing CO<sub>2</sub> flood. Crosswell seismic and electromagnetic data sets taken before and during CO<sub>2</sub> flooding of an oil reservoir are inverted to produce crosswell images of the change in compressional velocity, shear velocity, and electrical conductivity during a CO<sub>2</sub> injection pilot study. A rock properties model is developed using measured log porosity, fluid saturations, pressure, temperature, bulk density, sonic velocity, and electrical conductivity. The parameters of the rock properties model are found by an L1-norm simplex minimization of predicted and observed differences in compressional velocity and density. A separate minimization, using Archie's law, provides parameters for modeling the relations between water saturation, porosity, and the electrical conductivity. The rock-properties model is used to generate relationships between changes in geophysical parameters and changes in reservoir parameters. Electrical conductivity changes are directly mapped to changes in water saturation; estimated changes in water saturation are used along with the observed changes in shear wave velocity to predict changes in reservoir pressure. The estimation of the spatial extent and amount of CO<sub>2</sub> relies on first removing the effects of the water saturation and pressure changes from the observed compressional velocity changes, producing a residual compressional velocity change. This velocity change is then interpreted in terms of increases in the CO<sub>2</sub>/oil ratio. Resulting images of the CO<sub>2</sub>/oil ratio show CO<sub>2</sub>-rich zones that are well correlated to the location of injection perforations, with the size of these zones also correlating to the amount of injected CO<sub>2</sub>. The images produced by this process are better correlated to the location and amount of injected CO<sub>2</sub> than are any of the individual images of change in geophysical parameters.*

## **INTRODUCTION**

Crosswell seismic and electromagnetic technology has developed over the past two decades to provide high spatial resolution images of the seismic velocities (P and S) and electrical conductivity of the interwell region. The majority of effort, as measured by the topics of published and presented work, has concentrated on developing and improving

algorithms for estimating the geophysical parameters themselves (Newman, 1995; Lazaratos et al., 1995; Wilt et al., 1995; Nemeth et al., 1997; Goudswaard et al. 1998 to list but a few). In most applications where nongeophysical parameters, such as temperature during a steam flood (Lee et al., 1995) or CO<sub>2</sub> saturations during CO<sub>2</sub> flood (Harris et al., 1995; Wang et al., 1998) are the object of the crosswell survey, correlations between the geophysical parameters, e.g., velocity or electrical conductivity, and the desired reservoir parameter are derived and used to infer the distribution of reservoir parameters from the distribution of the geophysical parameters. The output from the survey is still most commonly a cross section of velocity, electrical conductivity or the time-lapse change of these parameters, which is then interpreted in terms of its implications for the distribution and/or change of the parameter of interest (temperature, CO<sub>2</sub> saturation, etc.).

The simple extension of interpreting the geophysical parameters themselves is to use relationships between geophysical and reservoir parameters (e.g., a regression fit between velocity and temperature) to convert a geophysical parameter to a reservoir parameter image. This approach can be used successfully in relatively simple reservoir systems with a minimum of fluid components and/or spatial variations in other controlling parameters (such as porosity, pressure, and temperature). However, in many settings the geophysical parameters depend on a number of reservoir parameters that are variable in both space and time. In particular, porosity, pressure, water, and gas saturation strongly influence seismic velocity. Electrical conductivity can generally be described as a function of porosity, water saturation, and fluid conductivity (Archie, 1942), although clay content may also need to be considered. As we will show, in a complex reservoir fluid system, the spatial distribution of the time-lapse change in geophysical parameters, such as velocity, can vary significantly from the spatial distribution of the time-lapse change in a desired reservoir parameter, such

as CO<sub>2</sub> saturation in oil. This difference results from the dependence of the geophysical parameters on more than one reservoir parameter (such as pressure and water saturation). These multiple dependencies must be sorted out before a picture of any single reservoir parameter can be obtained.

It has become common practice to use time-lapse changes in compressional and shear impedance mapped at the top of a reservoir. These changes are used to calculate time-lapse changes in effective pressure and water saturation within a reservoir without significant gas saturation (Landro, 2001). However, in systems where natural gas is present in significant concentrations or where gas in the form of CO<sub>2</sub> is introduced, quantitative prediction of pressure and fluid saturation changes becomes problematic because of trade-offs in the effects of the multiple reservoir parameters on the mapped geophysical parameters. The situation is further complicated if the objective is to monitor CO<sub>2</sub> injection into a reservoir already containing natural gas (in addition to oil and water).

The objective of the work described in this paper is to demonstrate a methodology of combining time-lapse changes in electric conductivity and compressional- and shear-wave velocity with a detailed rock-properties model, to produce quantitative estimates of the change in reservoir pressure, water saturation, and CO<sub>2</sub>/oil ratio.

## **THE FIELD EXPERIMENT**

Crosswell seismic tomography and electromagnetic imaging have been demonstrated in separate applications over the last decade. The SEG special issue 'Crosswell Methods' (Rector, 1995) contains several papers on the application of crosswell seismic tomography specifically for thermal process monitoring and several others on crosswell EM monitoring

of water floods. Wilt et al. (1995) report on the application of crosswell EM in water flood monitoring.

*In the fall of 2000 and spring of 2001 we conducted crosswell seismic and electromagnetic (EM) measurements in the Lost Hills oil field in southern California during a CO<sub>2</sub> injection pilot study by Chevron Petroleum Co. The objective of the pilot study was to demonstrate enhanced oil recovery resulting from CO<sub>2</sub> injection. We used this opportunity to study geophysical imaging of the reservoir during CO<sub>2</sub> injection.*

*The portion of the Lost Hills field where this experiment took place has been undergoing water flood since 1995. The CO<sub>2</sub> pilot covers four injection wells and surrounding producers.*

*Figure 1 shows the well placement in the affected portion of the*

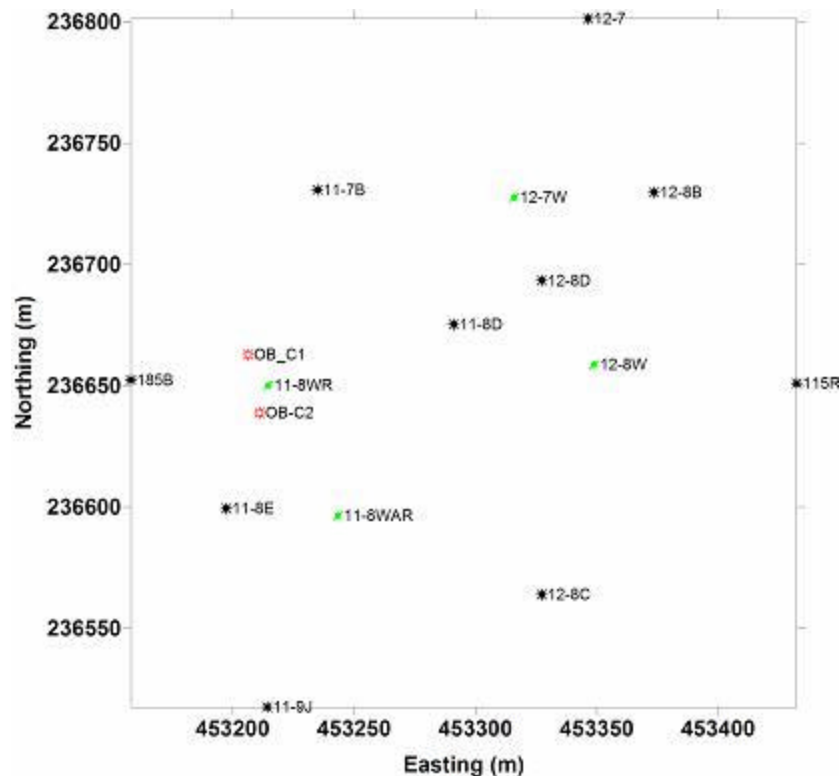


**Figure 1.** Area of the Lost Hills field affected by CO<sub>2</sub> injection. Four water injectors (shown in green) were converted to CO<sub>2</sub> injection in September 2000. The crosswell experiments took

*place between observation wells OB-C1 and OB-C2 (shown in red). A flow simulation production history match was done on the portion of the field covered by this figure.*

*field. Observation wells, OB-C1 and OB-C2, were drilled for the pilot and were fiberglass-cased to enable the use of crosswell EM. The nearby CO<sub>2</sub> injector (11-8WR) is located 20 feet out of the crosswell-imaging plane. These injection wells were hydraulically fractured to increase injectivity into the low-permeability diatomite reservoir. In some cases, downhole pressures were increased above the lithostatic pressure, which may have induced fracturing above the desired injection interval. If the fracture did indeed extend above the desired interval, much of the injected CO<sub>2</sub> would likely not sweep its intended target, but rather move into the higher section.*

The baseline crosswell seismic and EM surveys were conducted in September 2000, just prior to the beginning of CO<sub>2</sub> injection. A second EM survey was conducted in mid April 2001, and a second seismic survey was conducted in May 2001. In addition to the crosswell surveys, the two observation wells OB-C1 and OB-C2 were relogged for electrical resistivity in January 2001.

## **A ROCK-PROPERTIES MODEL**

*The reservoir parameters that have a dominant affect on geophysical parameters are porosity, pore pressure, effective pressure (lithostatic-pressure minus pore-pressure), fluid saturation, and the amount of dissolved hydrocarbon gas or CO<sub>2</sub> in oil. Pressure has a significant effect at Lost Hills because it is a shallow reservoir in soft rock. Converting geophysical images of the interwell region to reservoir parameters requires a rock-properties model relating the geophysical parameters to the reservoir parameters. We sought a model that would be able to predict observed velocity, density and electrical conductivity from observed pressure, porosity, and fluid saturations. Table 1 gives all the symbol definitions used in this*

paper. Laboratory measurements of the dry-frame moduli and grain density of the diatomite reservoir rock were unavailable, so to compute the seismic velocity we used the Hertz-Mindlin contact theory for the effective bulk ( $K_{dry}$ ) and shear ( $G_{dry}$ ) moduli of a dry, dense, random pack of spherical grains given by the following expressions:

$$K_{dry} = \left[ \frac{l^2 (1-f_0)^2 G_{grain}^2}{18p^2 (1-\nu)^2} \cdot P_{eff} \right]^{1/3} \quad (1)$$

$$G_{dry} = \frac{5-4\nu}{5(2-\nu)} \left[ \frac{3l^2 (1-f_0)^2 G_{grain}^2}{2p^2 (1-\nu)^2} P_{eff} \right]^{1/3}, \quad (2)$$

where  $\phi_0$  is the critical porosity (the porosity above which the grains become a liquid suspension),  $P_{eff}$  is the effective pressure,  $\nu$  is the grain Poisson's ratio,  $G_{grain}$  is the grain shear modulus and  $l$  is the average number of other grains each grain contacts. Equations (1) and (2) describe the effective dry-frame moduli at the critical porosity  $f_0$ . The modified Hashin-Shtrikman lower bounds (Hashin and Shtrikman, 1963) given by Dvorkin and Nur (1996),

$$K_{eff} = \left[ \frac{f/f_0}{K_{dry} + 4/3G_{dry}} + \frac{1-f/f_0}{K_{grain} + 4/3G_{dry}} \right]^{-1} - 4/3G_{dry} \quad (3)$$

$$G_{eff} = \left[ \frac{\mathbf{f}/\mathbf{f}_0}{G_{dry} + \frac{G_{dry}}{6} \left( \frac{9K_{dry} + 8G_{dry}}{K_{dry} + 2G_{dry}} \right)} + \frac{1 - \mathbf{f}/\mathbf{f}_0}{G + \frac{G_{dry}}{6} \left( \frac{9K_{dry} + 8G_{dry}}{K_{dry} + 2G_{dry}} \right)} \right]^{-1} \quad (4)$$

$$- \frac{G_{dry}}{6} \left( \frac{9K_{dry} + 8G_{dry}}{K_{dry} + 2G_{dry}} \right)$$

are used to model the dry frame moduli ( $K_{eff}$  and  $G_{eff}$ ) at porosity  $\mathbf{f}$ , where  $K_{grain}$  is the grain bulk modulus.

The bulk modulus of the fluid saturated rock ( $K_{sat}$ ) is modeled by Gassmann's equation (Gassmann, 1951) :

$$K_{sat} = K_{grain} \left[ \frac{\mathbf{f} \cdot K_{eff} - \left[ \frac{(1 + \mathbf{f}) \cdot K_{fluid} \cdot K_{eff}}{K_{grain}} \right] + K_{fluid}}{(1 + \mathbf{f}) \cdot K_{fluid} + \mathbf{f} \cdot K_{grain} - \left[ \frac{K_{fluid} \cdot K_{eff}}{K_{grain}} \right]} \right], \quad (5)$$

where  $K_{fluid}$  is the aggregate bulk modulus of the fluids filling the pore space. The bulk shear modulus of the fluid saturated rock is assumed to equal that of the dry rock.

The possible fluids filling the pore space are oil, brine, hydrocarbon gas, and  $CO_2$ . A common approach for calculating  $K_{fluid}$  is to use Wood's mixing formula (Wood, 1955):

$$1/K_{fluid} = S_w / K_{brine} + S_{oil} / K_{oil} + S_{hcg} / K_{hcg} + S_{co2} / K_{co2}, \quad (6)$$

where the water saturation ( $S_w$ ), oil saturation ( $S_{oil}$ ), hydrocarbon gas saturation ( $S_{hcg}$ ) and  $CO_2$  saturation ( $S_{CO_2}$ ) sum to 1.0. The bulk moduli of brine, oil, hydrocarbon gas, and  $CO_2$  are  $K_{brine}$ ,  $K_{oil}$ ,  $K_{hcg}$ , and  $K_{CO_2}$ , respectively. We will discuss this method of calculating  $K_{fluid}$  at the end of this section.

The bulk density is given by a simple mixing law

$$\mathbf{r}_{bulk} = (1-f) \mathbf{r}_{grain} + f(1-S_{hcg} - S_w - S_{CO_2}) \mathbf{r}_{oil} + fS_w \mathbf{r}_{brine} + fS_{hcg} \mathbf{r}_{hcg} + fS_{CO_2} \mathbf{r}_{CO_2}, \quad (7)$$

where  $\mathbf{r}_{grain}$ ,  $\mathbf{r}_{oil}$ ,  $\mathbf{r}_{brine}$ ,  $\mathbf{r}_{hcg}$ , and  $\mathbf{r}_{CO_2}$  are the grain, oil, brine, hydrocarbon gas, and  $CO_2$  densities, respectively, as a function of pressure and temperature.

The fluid bulk moduli  $K_{brine}$ ,  $K_{oil}$ ,  $K_{hcg}$  and densities  $\mathbf{r}_{brine}$ ,  $\mathbf{r}_{oil}$ ,  $\mathbf{r}_{hcg}$  of the brine, oil, and hydrocarbon gas respectively are computed using relations from Betzel and Wang (1992). The bulk modulus and density of  $CO_2$ ,  $K_{CO_2}$  and  $\mathbf{r}_{CO_2}$ , respectively, as well as the bulk moduli and densities of  $CO_2$ -hydrocarbon gas mixtures, are modeled using relations from Magee and Howley (1994).

The bulk electrical conductivity ( $\mathbf{S}_{bulk}$ ) of the reservoir rock is modeled using Archie's (1942) relationship

$$\mathbf{S}_{bulk} = \mathbf{S}_{brine} \cdot f^m \cdot S_w^n, \quad (8)$$

where  $\mathbf{S}_{brine}$  is the fluid conductivity, and  $m$  and  $n$  are numbers usually between 1 and 3.

The model parameters in Equations (1) through (7) were found by using a simplex algorithm to minimize  $L_1$  given by Equation (9).

$$L_1 = \sum_1^N (V_p^{obs} - V_p^{calc}) + \sum_1^N (\mathbf{r}^{obs} - \mathbf{r}^{calc}), \quad (9)$$

where  $V_p^{obs}$ ,  $V_p^{calc}$ ,  $\mathbf{r}^{obs}$ , and  $\mathbf{r}^{calc}$  are the sonic log compressional velocity, model calculated sonic compressional velocity, log density, and model calculated density, respectively. The units used in defining  $L_1$  were m/s and Kg/m<sup>3</sup>, so that the velocity and density had approximately equal numerical magnitude, and hence equal weight in the value of  $L_1$ . Because the observation wells used in the crosswell surveys did not have full logging suites (no sonic logs), the nearest well (1,000 ft away) with a full suite of logs was used. Electrical parameters in Equation (8) were determined by a regression using the OB-C1  $\mathbf{s}$ ,  $\mathbf{f}$ , and  $S_w$  logs. Predicted  $V_p$ ,  $\mathbf{r}$ , and  $1/\mathbf{s}$  compared to the observed logs are shown in Figure 2, with the model parameters determined from the regressions listed in Table 2.

Parameters listed in bold type in Table 2 (critical porosity, oil API gravity, brine salinity, and temperature) were held fixed in the regression. These values, with the exception of critical porosity, came from direct measurement. Although we are not interested in the model parameters per se (we are only interested in the model's ability to predict  $V_p$ ,  $V_s$ , and  $\mathbf{r}$ , given reservoir parameters), note that their values are quite realistic. The gas density  $G$  is very close to that of methane. Estimated shear modulus and grain density of the diatomite grains is very

close to the values of 18 (GPa) and 2.3 (g/cc) estimated by Wang (2001). Bilodeau (1995) measured an average grain density of 2.37 g/cc from another location in the diatomite at Lost Hills; he also measured -1.84, -1.95, and 0.21 (S/m) for Archie's Law porosity exponent, saturation exponent and fluid conductivity, respectively, on the same samples. A value of critical porosity was determined by a set of minimizations of Equation (9) where  $\phi_0$  was varied between 0.5 and 0.7, all of which reached essentially the same value of  $L_1$ . The value of  $\phi_0$  was chosen that resulted in values of  $G_{\text{grain}}$  and  $\rho_{\text{grain}}$  that were close to those estimated by Wang (2001).

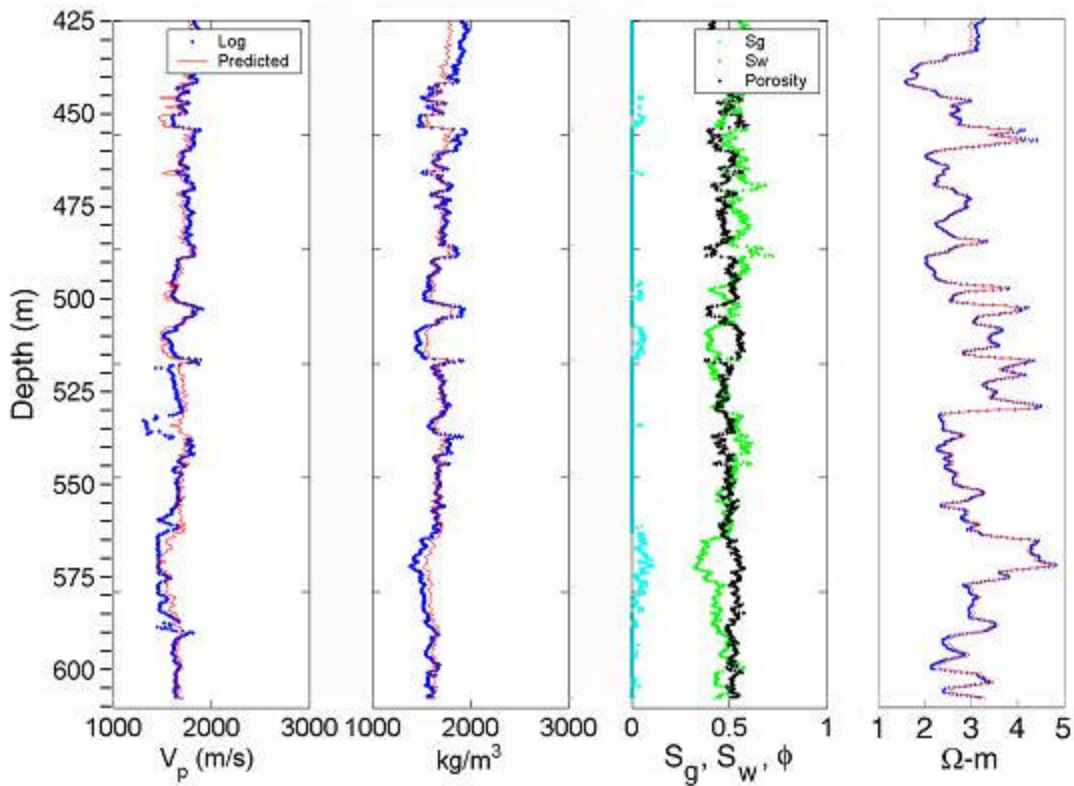


**Figure 2.** Rock properties model uses logged porosity (black), water saturation (green) and gas saturation (light blue) as inputs in a multi-parameter regression to predict the velocity (left panel), density (second from left panel) and electrical resistivity (right panel). Measured velocity, density, and resistivity are shown in blue; model predicted values are shown in red.

*In Table 1, only one parameter, “gas correction”, is listed under the Gassmann fluid substitution column. In addition, the Gassmann formula uses the dry-frame modulus as well as the fluid bulk moduli derived from the Batzle and Wang (1992) relations. However, we found that to fit the observed velocity in areas where the gas saturation was non-zero, the gas effect had to be reduced. The overestimation of the gas effect on fluid bulk modulus by the Wood’s mixing law, Equation (6), has been observed by Brie et al. (1995). A better match between predicted and observed velocity could be achieved by a simple correction to the gas term in Equation (6), yielding a modified equation*

$$K_{fluid} = 1.0 / \left[ G_c * (S_{hcg} / K_{hcg}) + (S_w / K_{brine}) + \left( (1 - S_{hcg} - S_w - S_{CO2}) / K_{oil} \right) + (S_{CO2} / K_{CO2}) \right] \quad (10)$$

*where  $G_c$  is the gas correction listed in Table 1.*

*The pressure prediction capability of the model was validated by comparison to measurements made by Wang (2001) on core samples of diatomite from Lost Hills. Figure 3 shows the measured compressional velocity for vertical and horizontal propagation. These measurements show a horizontal-to-vertical velocity anisotropy of 1.047 that varies slightly as a function of pressure. We will come back to the velocity anisotropy when we consider the velocity inversion of the crosswell data.*

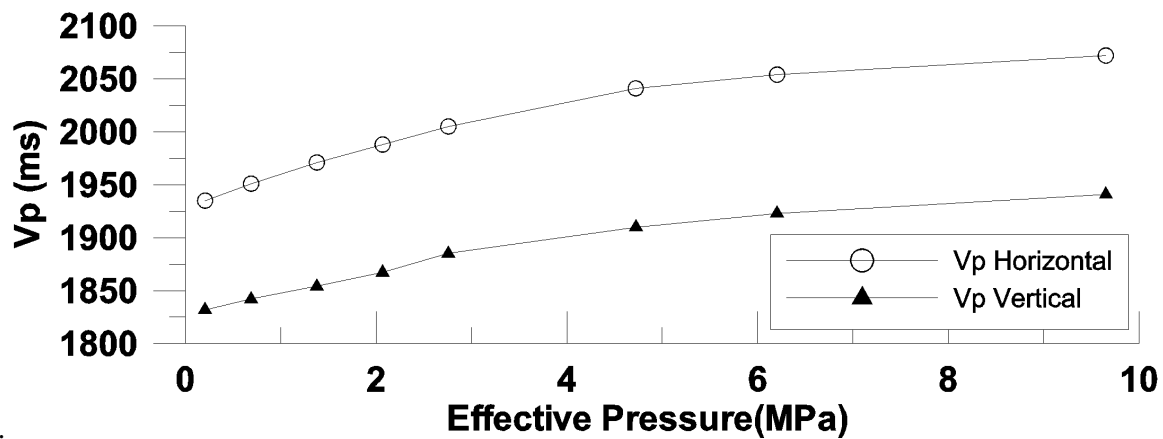


**Figure 3** Vertical and horizontal compressional velocity as a function of effective pressure measured on Lost Hills Diatomite core by Wang (2001). Core was saturated with 19 API oil and 200,000 ppm brine (50-50 ratio) at 22.7 C.

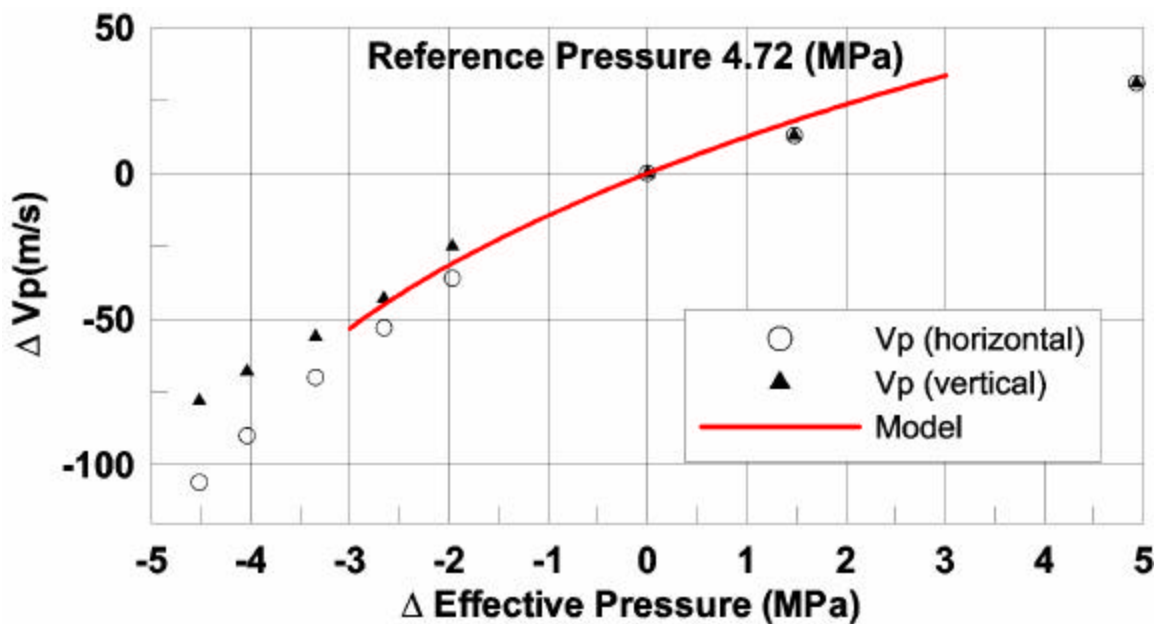


**Figure 4.** Predicted velocity change as a function of change in effective pressure compared to laboratory measurements on Lost Hills diatomite core samples.

*Figure 4 presents the data from Figure 3 recast as velocity changes as a function of pressure changes at a reference pressure of 4.7 MPa, the average effective pressure in the reservoir at the start of CO<sub>2</sub> injection. For expected decreases in effective pressure (increases in pore pressure)*

*in the range 0 to 3 MPa from the reference pressure, the rock properties model predictions are within a few percent of the lab measurements vertical velocity. The rock-properties model is derived from log sonic measurements dominated by vertical propagation along the borehole, so the correspondence to the vertical core measurements is expected. For changes in effective pressure above the reference pressure, the lab measurements show a change in the slope of the curve, with the quality of the fit between model and lab data decreasing. The difference in this region is probably associated with pore crushing in the lab samples not accounted for in the rock-properties model.*

*The estimates of the time-lapse changes in geophysical parameters derived from inversion of the observed geophysical data, as described in the following sections, are used with the rock-properties model described by Equations (1)–(5), (7), (8), and (10), with constants listed in Table 2, to calculate time-lapse changes in reservoir parameters.*

### **INTEGRATED TIME-LAPSE GEOPHYSICAL IMAGES**

*The algorithms, assumptions, starting models, and amount of incorporated a priori information all greatly affect the velocity and conductivity models resulting from inversion. Inversions of the individual data sets done separately, without any mechanism for linking the models, produces images of  $V_p$ ,  $V_s$ , and  $\mathbf{s}$  with little spatial correlation. Since we assume that the changes in reservoir parameters affect all of the geophysical parameters (albeit in different ways), we expect a certain degree of spatial correlation between changes in the different geophysical parameters. This assumption acts as a constraint on the possible solutions. In this experiment, sonic logs were not run in OB-C1 or OB-C2, but conductivity logs were run in both wells. The strategy we adopted to maximize the spatial correlation between velocity and conductivity images was to begin with the EM data, where the greatest amount of a priori information existed, and then use the conductivity image to produce a starting  $V_p$  model,*

*followed by producing a starting  $V_s$  model from the final  $V_p$  model. Conductivity logs were used to build the starting conductivity model for the EM inversion. The EM inversion algorithm is described by Newman (1995). We chose to use the conjugate gradient algorithm of Jackson and Tweeton (1996) for the travel-time tomography because the final model is sensitive to the initial model and is perturbed from the starting model only as much as needed to fit the observed data. Both EM and seismic inversions models were parameterized by 3 m cells.*

*EM inversion for the data at initial conditions (late August 2000 before  $CO_2$  injection) was started from a model built by laterally interpolating the conductivity logs between the OB-C1 and OB-C2 wells. The final inversion model from this data was then used as the starting model for the inversion of the April 2001 data. The difference of the two inversions provides the time-lapse change in conductivity shown in Figure 5c. A high degree of correlation exists between the permeability log from the injector and the areas where the largest decrease in conductivity occurs. The correlation between high permeability and large changes in conductivity (water saturation) is expected.*

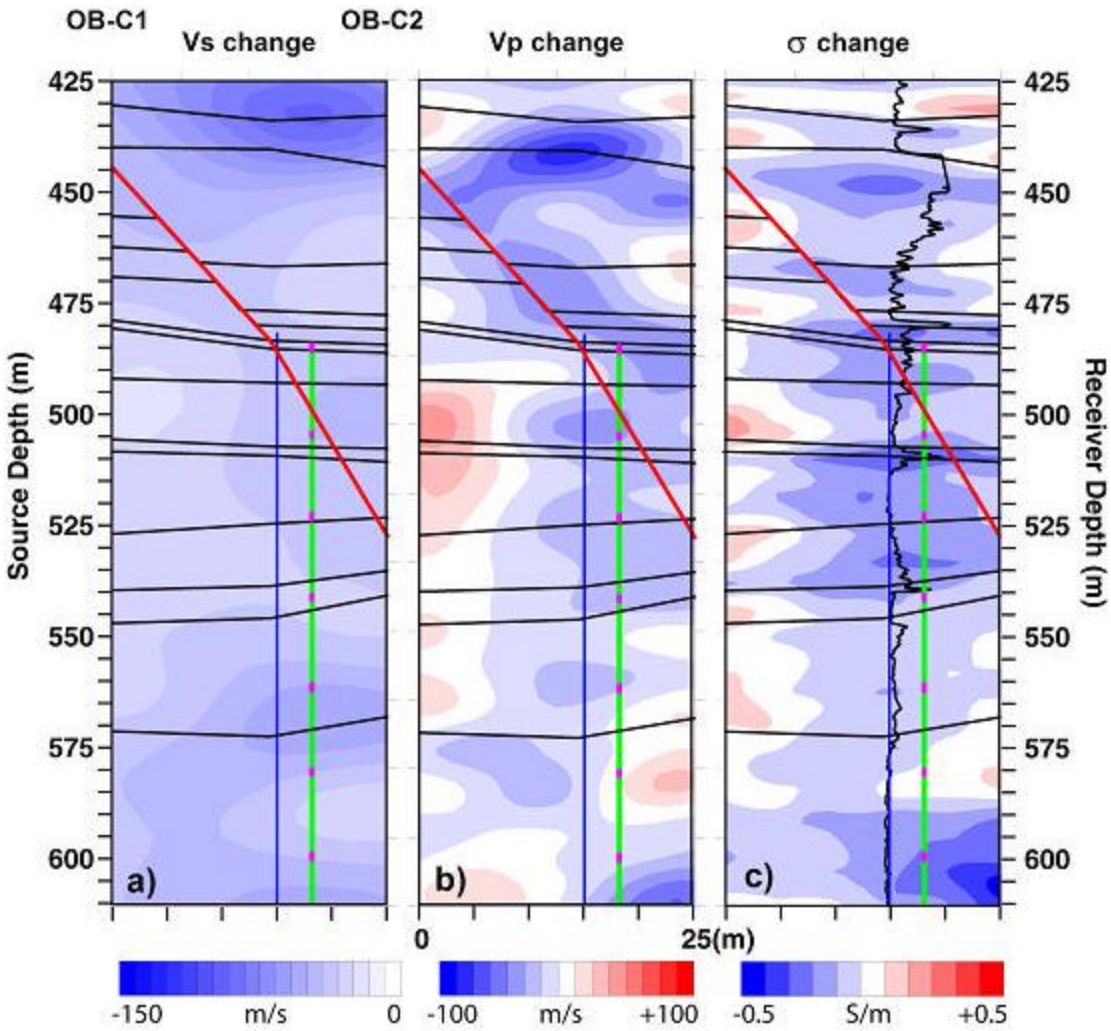


**Figure 5.** Time-lapse changes in (a) shear velocity, (b) compressional velocity and (c) electrical conductivity. The EM images were used to construct starting models for the  $V_p$  inversions; the resulting  $V_p$  images were used to construct starting models for the  $V_s$  inversions. Major unit boundaries are shown as black sub-horizontal lines, estimated location of previous water injection fracture is shown as a vertical blue line, estimated location of the  $\text{CO}_2$  injection fracture is shown as a vertical green line, perforation intervals for  $\text{CO}_2$  injection are shown as magenta dots, and the mapped location of a fault zone is shown as the red diagonal line. The permeability log in the out-of-plane  $\text{CO}_2$  injection well (11-8WR) is shown in black on panel (c).

*Next, the conductivity models from the two inversions were converted to compressional velocity. Values of  $f$ ,  $P_{eff}$ ,  $P_{pore}$ , and  $S_{hcg}$ , based on averages from the log data, were used with*

regression derived parameters (Table 2) to calculate  $V_p$  and  $\mathbf{S}$  as a function of  $S_w$ , using Equations (1)-(5), (7), (8), and (10). A linear regression between the calculated  $V_p$  and  $\mathbf{S}$  was done to provide a function for converting  $\mathbf{S}$  to  $V_p$ . The converted  $\mathbf{S}$  models were then used as initial models in the inversion of the  $V_p$  travel-time data to produce the change in  $V_p$  shown in Figure 5b. In addition to a decrease in  $V_p$  in the region around the estimated locations of the old water and new  $CO_2$  injection fracture locations, there are decreases in  $V_p$  that align with the upper section of the mapped fault, implying that  $P_{pore}$  increases along the upper section of the fault. Since there are few conductivity changes associated with the fault, these results indicate that pressure changes occur along the fault zone without significant changes in water saturation at the time of the experiment.

The largest  $\mathbf{S}$ ,  $V_p$ , and  $V_s$  changes occur in a region bordered by the old water injection fracture and the new  $CO_2$ -injection fracture. The water injection was ongoing for more than six years and likely produced a high-permeability damage zone that has been intersected by the newer  $CO_2$  fracture. We speculate that this has produced a relatively high permeability zone in the region between and surrounding the two ideal fracture locations. Both the conductivity and  $V_p$  change sections (Figure 5c and 5b) show an increase in conductivity and  $V_p$  near the OB-C1 and OB-C2 wells. This is caused by an increase in water saturation, as shown in the relogging of the wells in January 2001. Water moving outward and away from the high permeability injection zone as  $CO_2$  is injected causes a “rind” of increased  $S_w$  surrounding the volume affected by  $CO_2$ . The volume of rock affected by  $CO_2$  injection will have reduced water content as either  $CO_2$  fills the pore space or oil absorbs  $CO_2$  and swells, expelling water. This volume will have a surrounding “rind” of increased water saturation.

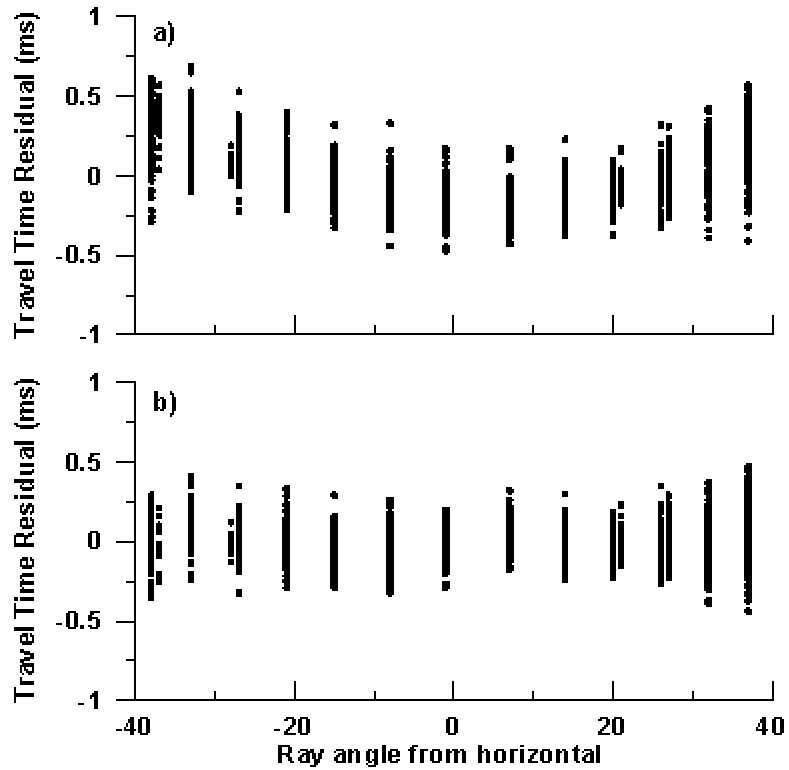


**Figure 6.** *Travel time residual (observed – calculated) vs. ray angle from horizontal. Panel (a): homogeneous halfspace starting model with no anisotropy or dip of the velocity field. Panel (b): homogeneous halfspace starting model with  $V_{horizontal}/V_{vertical} = 1.05$  and symmetry axis 7 degrees from vertical.*

*The algorithm (Jackson and Tweeton, 1996) used to produce the velocity tomograms shown in Figure 5 allows setting a constant velocity anisotropy and a constant dip of the anisotropy symmetry axis for the entire cross section. In a series of tomographic inversions, values of the horizontal/vertical velocity and the dip of the symmetry axis were varied between 0.9 and 1.1 and  $-10$  to  $+10$  degrees, respectively. The final values of 1.05 and 7 degrees from vertical (respectively) used in Figure 5 produced the flattest travel-time misfit-versus-ray angle scatter plot with the minimum RMS data misfit. Figure 6a shows the travel-time residual plot for a  $V_p$  model without anisotropy, and Figure 6b shows the residual for the final  $V_p$  model shown in Figure 5b. The horizontal-to-vertical velocity ratio of 1.05 from the crosswell seismic tomograms compares remarkably well with the value of 1.047 from core measurements shown*

earlier in Figure 3. In addition, the structural dip of the reservoir units in the plane of the crosswell experiment is 7 degrees.

The starting models for the  $V_s$  inversions were converted from the final  $V_p$  sections using a  $V_p/V_s$  ratio derived from the rock properties model. The final  $V_s$  models were differenced to produce the change in  $V_s$  section shown in Figure 5a. The  $V_s$  change section is much smoother than either the conductivity or  $V_p$  change sections. This results partially from the lower frequency content in the shear-wave data. Shear-wave data were acquired using an orbital vibrator source with a center frequency of 500 Hz, whereas the compressional wave data were acquired using a piezoelectric source with a center frequency of 2,000 Hz. The  $V_s$  change section is also smoother because  $V_s$  is relatively insensitive to changes in water saturation (which have high spatial variability) and more sensitive to pressure changes (which have much lower spatial variability). Even with the smoother spatial changes in  $V_s$  we see a correlation with  $V_p$  and conductivity changes. In particular, the zone along the fault shows a decrease in  $V_s$ , lending support to our interpretation that pore pressure is increasing along the fault zone.

### **THE EFFECTS OF GAS ON SEISMIC VELOCITY AND DENSITY**

The goal is to predict changes ( $\Delta$ ) in reservoir pressure, fluid saturations, and the amount of absorbed CO<sub>2</sub> in the oil as the CO<sub>2</sub> flood proceeds. We assume that the porosity remains constant over the time of the experiment. To use the rock-properties model to predict changes in reservoir parameters from changes in geophysical parameters, we must define certain values for reference parameters with respect to which the changes will be computed. In particular, reference water saturation ( $S_w$ ) and porosity ( $\phi$ ) of 0.5 and 0.52, respectively, are taken from the averages in the OB-C1 well over the reservoir interval prior to CO<sub>2</sub> injection. The reference pore pressure ( $P_{\text{pore}}$ ) is taken from a history-matched flow simulation model at the beginning of CO<sub>2</sub> injection. The reference effective pressure ( $P_{\text{eff}}$ ) on the rock frame for seismic velocity calculations is calculated from the integrated density log minus  $P_{\text{pore}}$ . We will consider the sensitivity of our predictions to values of the reference parameters below.

Both hydrocarbon gas and CO<sub>2</sub> in the reservoir affect the seismic velocities through three possible mechanisms:

- (1) by directly changing the bulk modulus of the composite fluid in the pore space as gas saturation changes (Equation 10).
- (2) By changing the bulk modulus of the oil as the amount of dissolved gas changes.

(3) By changing the bulk density of the rock.

Equation (11), from Batzle and Wang (1992), gives the maximum amount of gas that can dissolve in oil expressed as a gas/oil ratio ( $R_G^{\max}$ ) as a function of pore pressure ( $P_{\text{pore}}$ ), temperature in degrees Celsius (T), oil API gravity (API), and gas gravity ( $G_{\text{grav}}$ ):

$$R_G^{\max} = 2.03G_{\text{grav}} \left[ P_{\text{pore}} \exp(0.02878\text{API} - 0.00377T) \right]^{1.205} \quad (11)$$

The gas/oil ratio is the volume ratio of liberated gas to remaining oil at atmospheric pressure and 15.6° C. Batzle and Wang (1992) also provide formulas for computing the velocity and density of oils with dissolved gas, which we have used in our calculations.

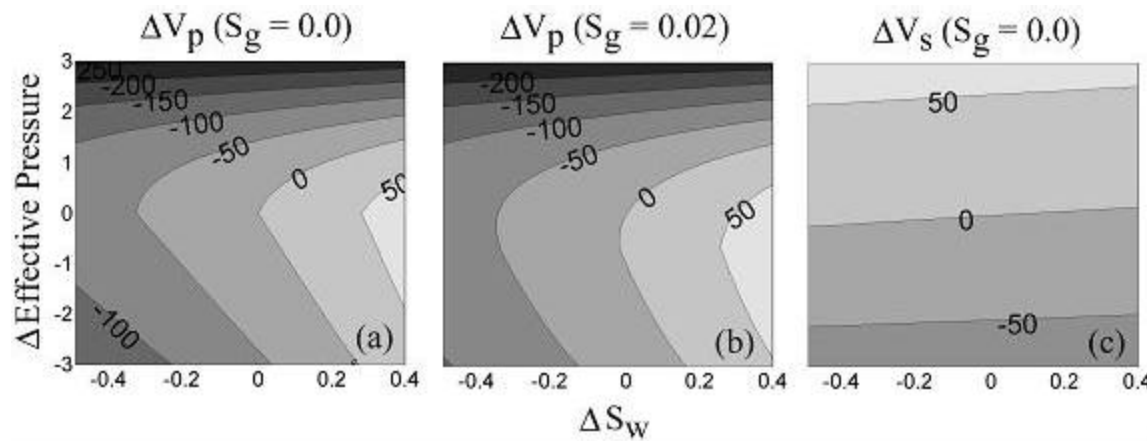


**Figure 7.** Change in velocity (m/s) as a function of change in effective pressure and water saturation at reference values of  $S_w=0.5$ ,  $S_{\text{hcg}}=0.0$ ,  $f = 0.52$  and  $P_{\text{eff}}=4.7\text{MPa}$ . Panel (a)  $DV_p (S_{\text{hcg}} = 0.0)$  (b)  $DV_p (S_{\text{hcg}} = 0.02)$  (c)  $DV_s (S_{\text{hcg}}=0.0)$ . The oil contains the maximum amount of dissolved hydrocarbon gas as a function of pressure for the parameters of the rock properties model given in Table 1.

An increase in the amount of dissolved gas in the oil, as measured by  $R_G$ , decreases both the bulk modulus and density of the oil. The bulk modulus is reduced more than the density, resulting in a decrease in the compressional velocity of the oil. Figures 7a and 7c show the calculated  $\Delta V_p$  and  $\Delta V_s$  using oil with the maximum amount of dissolved hydrocarbon gas as functions of  $\Delta P$  and  $\Delta S_w$ , at a reference point (reservoir just prior to  $\text{CO}_2$  injection) where  $S_w$ ,  $S_{\text{hcg}}$ ,  $\phi$ , and  $P_{\text{eff}}$  are equal to 0.5, 0.0, 0.52, and 4.7 (MPa), respectively. When  $S_{\text{hcg}}$  is non-zero and free gas exists, the behavior of  $\Delta V_p$  with  $\Delta P$  and  $\Delta S_w$  changes markedly. Figure 7b shows  $\Delta V_p$  for the same reference values as Figure 7a, but with  $S_{\text{hcg}} = 0.02$ . Equation (11) is used to compute the maximum amount of dissolved gas as a function of pressure. As  $P_{\text{pore}}$  increases above the reference pressure,  $R_G^{\max}$  increases, and we assume that *in situ* gas will dissolve into the oil up to  $R_G^{\max}$ . As the pressure decreases below the reference pore pressure,  $R_G^{\max}$  decreases, and gas will come out of solution, thereby increasing  $S_{\text{hcg}}$  above its reference value. This